X-RAY COMPUTED TOMOGRAPHY OF DAMAGE FORMATION UNDER IN-SITU LOADING

A. Sandhu[1], L. Glen[1], M. Doughty[1], A. T. Rhead[1]

[1]Department of Mechanical Engineering, University of Bath
Claverton Down, Bath, BA2 7AY, UK
Email: atr21@bath.ac.uk, web page: http://www.bath.ac.uk/mech-eng

Keywords: In-situ loading, X-ray CT, Damage, Impact

ABSTRACT

Use of X-ray Computed Tomography (XRCT) to investigate damage morphology has previously been constrained to post-test analysis of unloaded coupons. As delaminations and intra-ply cracks close when load is removed, a limit is placed on the information available for identifying mechanisms causing resin and fibre fracture. Here, a newly developed loading stage, for in-situ XRCT imaging of laminates under quasi-static impact loading, is employed to visualise the mechanisms that drive the formation of damage morphologies. Multiple X-ray CT scans taken at increasing indenter displacements reveal the evolution of damage morphology. Various laminates subject to out-of-plane, near-edge or on-edge impacts are assessed. For out-of-plane and on-edge impact, both a conventional and novel stacking sequence are considered. Favourable formation mechanisms that occur in laminates with novel sequences are highlighted. In particular, damage from out-of-plane impacts is seen to occur in two stages. The first stage is instantaneous, with multiple shear-driven intra-ply cracks and inter-ply delaminations occurring at plies with dissimilar interfaces. In the second stage, shear-driven cracking gives way to peeling of layers. This peeling is focussed at certain weaker interfaces and is driven by an intact core of material pushing through the laminate. The latter process is clearly demonstrated by testing of a laminate with stacking sequence $[0_4/90_4]_s$. Results indicate that stacking sequence can be used to force the development of favourable damage morphologies that protect load carrying plies and prevent the near surface delaminations which enable sublaminate buckling driven failures.

1 INTRODUCTION

Owing to the significant reduction in residual strength that it can cause, both academic and the aerospace industry have undertaken extensive research into impact damage of CFRP laminates [1-14]. Of this damage, Barely Visible Impact Damage (BVID) is particularly dangerous because it is difficult to detect in service. Despite this research effort and multiple competing theories to describe them, there is currently limited understanding of the mechanisms that determine impact damage morphology [6,7,10-13]. This is partially a consequence of the dynamic nature of impact and the comparatively long scan-times required by NDE techniques capable of inspecting internal damage, e.g C-scan and X-ray Computed Tomography (XRCT). As such NDE of damaged laminates has previously been constrained to post-test analysis of unloaded coupons [1,2,15]. As delaminations and intra-ply cracks close when load is removed, some information is lost in standard NDE tests making it difficult to identify mechanisms that shape damage morphology. However, at the low velocities at which BVID typically forms, laminate response is dominated by the lowest mode shape implying that load, deflection and hence, the strain are effectively in the same phase. As such, quasi-static loading is a good approximation of the low velocity impacts that typically produce BVID [3-5].

Here, a newly developed rig for in-situ XRCT of laminates under load has been used to observe the formation of damage during quasi-static impact testing of laminates with both standard angles and non-conventional angle plies. This paper explores the use of in-situ XRCT to visualize and describe mechanisms that drive the creation of intra-ply cracks and delamination growth in laminates subject to both out-of-plane and in-plane quasi-static impact loading.

2 COUPON DESIGN AND MANUFACTURE

Six different coupons were manufactured to allow investigation of on-edge, near edge and out-of-plane impact. The stacking sequence and geometry of the coupons are presented in Table 1. All samples were manufactured from M21/T800, unidirectional prepreg with ply thickness 0.25mm and material properties E_{11} = 172GPa, E_{22} = 8.9GPa, G_{12} = 4.2GPa and ν_{12} = 0.35 [16].

Code	Layup	Thickness(mm)	Impact type	Shape
$[(\pm60)_3]$OE	$[(\pm60)_3/(\pm5)_5]_s$	8.2	On edge	Rectangular
$[(\pm45/0_2]$OE	$[(\pm45/0_2/90/0_2)_2/\pm45]_s$	8.26	On edge	Rectangular
$[0_4]$OP	$[0_4/90_4]_s$	4	Out-of-plane	Circular
[±45/0/90]OP	$[\pm45/0/90/0/\mp45/0]_s$	4.03	Out-of-plane	Circular
$[(\pm45)_2]$OP	$[(\pm45)_2/0_3/90/0]_s$	4.45	Out-of-plane	Circular
$[(\pm45/0_2]$NE	$[(\pm45/0_2/90/0_2)_2/\pm45]_s$	8.22	Near edge	Semi-circular

Table 1: Laminate codes and layups.

Stacking sequences were chosen to reflect typical wing skin and stiffener ply percentages. Stacking sequence variations are considered in order to highlight the potential for manipulation of damage morphology. [±45/0/90]OP comprises a typical homogenised laminate with a ply percentage of 40/50/10 distribution of 0°, 45° and 90°, respectively. $[(\pm45)_2]$OP has a more typical 44/44/12 wing skin ratio with a blocked damage tolerant layup [17]. Owing to the likely sources of in-service impacts (e.g. runway chippings and tool drops), these coupons were subjected to a central out-of-plane impact.

$[(\pm45/0_2]$OE and $[(\pm45/0_2]$NE represent typical stiffener designs with a homogenised stacking sequence comprised of standard ply angles in the ratio 50/40/10. $[(\pm60)_3]$OE is a unique design based on a stiffener patent by Boeing [18]. Since stiffeners primarily experience edge or near edge impacts [8,9], rectangular coupons were subjected to quasi-static on-edge impacts and the semi-circular sample to near edge impact.

Laminates were manufactured according to the manufacturer's recommended cure cycle. As cured laminates were square with sides measuring 120mm but were subsequently machined down to achieve uniform edges. Circular test coupons measured 100mm in diameter and rectangular test coupons measured 110mm by 100mm, see Fig. 1. Figure 2(a) shows the geometry of the semi-circular coupon.

3 METHOD

3.1 LOADING STAGE DESIGN AND OPERATION

Figures 1 and 2 show cross-sections of the purpose built quasi-static loading stage as adapted for in-plane and near edge impacts (Fig. 1(a), Figs 2(a) and (b)) and on-edge impact (Fig. 1(b) and Fig.2 (c)). The loading stage comprises an indenter, clamped coupon supports and load cell as its major parts. The housing (outer tube) and the impactor are made of CFRP making them relatively transparent to X-rays.

The CFRP supports shown in Figure 1(a) and 1(b) are contained within a concentric CFRP tube. Both the supports and tube are 5mm thick. The CFRP housing is bounded by steel plates on both ends. In the out-of-plane and near-edge impact configurations, axial compressive load is applied to the support rings by the internal indenter housing, creating a clamped boundary condition around the circumference of the sample. For the in-plane impact configuration, rings are swapped for semi-cylindrical supports. These are slit along their vertical axis in order to provide out-of-plane support to the rectangular coupon required for the in-plane impact, see Fig. 1(b).

In the zero load position, the indenter sits on the top edge of the coupons as shown in Figs 1 and 2. To create a quasi-static impact load the indenter is driven into the coupons using the loading screw that

extends beyond the top steel plate. When a load is applied, the reaction force on the indenter pushes the loading structures away from each other creating a tensile reaction load in the external CFRP tube.

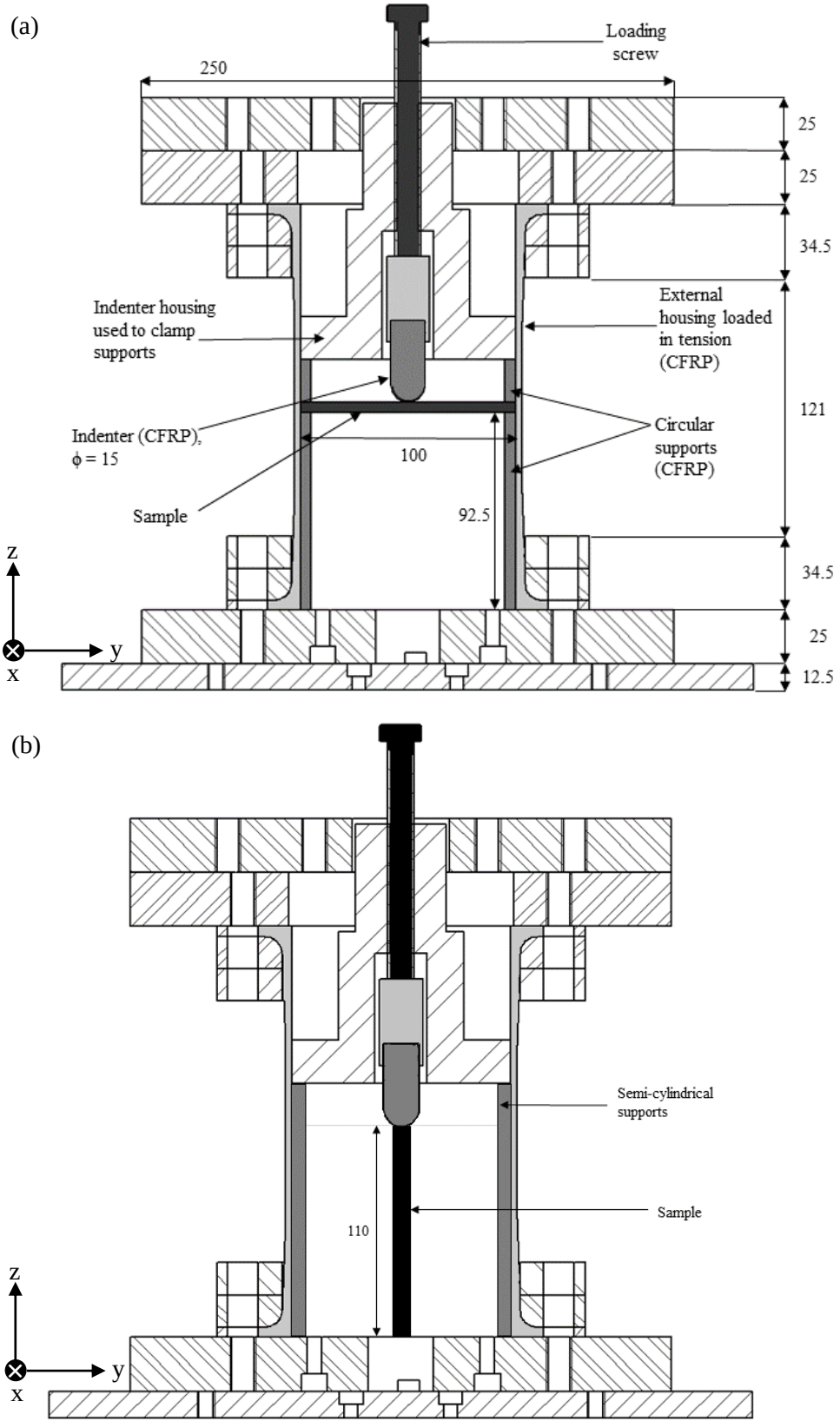

Figure 1: Cross-section of the load stage; (a) with a horizontal circular coupon for front and near edge impact; (b) with a vertical rectangular coupon for on-edge impact.

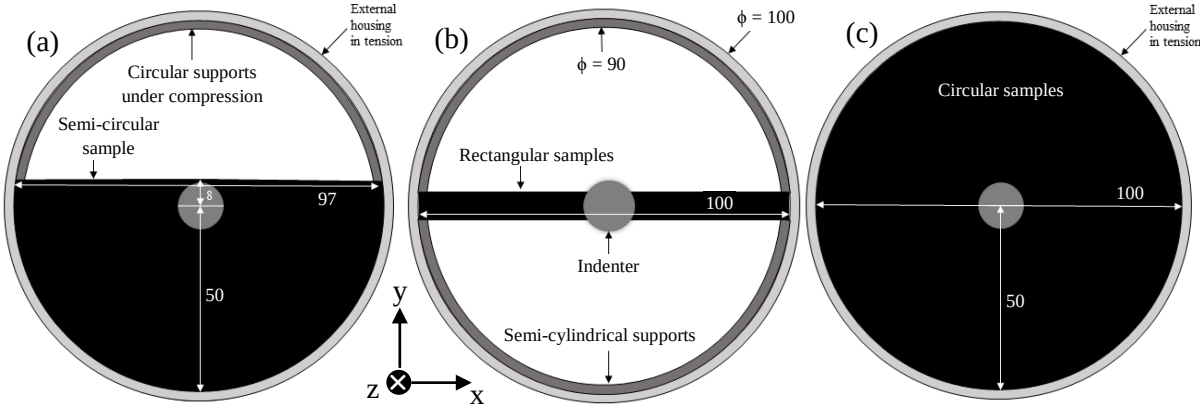

Figure 2: Cross sectional plan view of the jig showing housing, supports, indenter and coupons; (a) Near edge impact on the semi-circular $[(\pm 45/0_2]$NE coupon; (b) Edge impact on the $[(\pm 60)_3]$OE & $[(\pm 45/0_2]$OE rectangular coupons; (c) Out-of-plane impact on circular coupons. All dimensions in mm.

3.2 QUASI-STATIC IMPACT TEST METHOD AND XRCT

The loading screw is used to apply incremental increases in indenter displacement. Each displacement is held for 255 minutes, the time required to XRCT scan the sample. In order to determine the order of damage progression, all coupons were scanned under zero load and then at two further indenter displacements; vertical displacement being measured using XRCT data. It is noted that there was no evidence of rigid body movement of the sample relative to its fixture during scanning and that the loading stage remained locked in position in the XRCT scanner throughout all applications of load. Displacement was halted after either initial audible cracking or, for the second displacement stage, after extensive audible cracking. XRCT scans were taken prior to loading and at the end of each displacement phase using a Nikon XT H 225 ST CT scanner with a Tungsten target and Perkin Elmer 1620 16-bit, 2000 by 2000 pixel detector. The system has a 225kV microfocus source with a minimum 3μm spot size. 3600 projections were taken per scan with each projection being a composite of the average of 4 images. Images were taken with 708ms exposures under x-ray conditions of 140kV and 242 μA.

To improve the signal to noise ratio, the loading stage was inclined at approximately 7.5° for circular and semi-circular samples. This minimised the number of projections in which X-rays must travel through the full diameter of the coupon. After reconstruction, scans were processed using Avizo Fire 8.0 visualisation software [19].

4 RESULTS

Figures 3(a)-(c) show three dimensional views illustrative of the different indenter/coupon configurations following the second indenter displacement for the [±45/0/90]OP, $[(\pm 60)_3]$OE and [(±45/02]NE coupons respectively. Cross-sectional and 3 dimensional videos of all the tests shown in Figs 3-9 can be found using either the QR code in Fig. 4 or DOI: 10.15125/BATH-00093. QR reader software is readily available for all major mobile phone operating systems. Blurring at the edges of images is a consequence of the weight of the rig (43kg) causing eccentricity in the rotation of the sample.

Figures 4(a)-(c) show the progression of damage during near edge loading of the $[(\pm 45/0_2]$NE coupon parallel to the 0° axis. Figure 4(d) shows a cross-section through the impact centre parallel to the 90° axis during the second displacement of the indenter. Damage is seen to initiate asymmetrically about the indenter mid-line at the free edge during the first displacement of the indenter, see point 1 Fig. 5 (b). Delamination during the second stage of the $[(\pm 45/0_2]$NE coupon (Figs 4(c) and (d)) is drawn to the free-edge region already compromised by the initial damage event. New delaminations (points 2-4) and intra-ply cracks appear closer to the indenter contact point and the significant initial delamination (point 1) has begun to extend beneath the indenter, see Fig. 5(d).

Figure 5 shows the in-situ out-of-plane loading of a $[0_4]$OP laminate. The simple stacking sequence of this coupon produces a simple damage mechanism. Intra-ply cracking gives rise to independent 'beams' that have peeled away from each other. Peeling of these beams creates pairs of orthogonal delaminations that lie just outside the intact laminate region directly under the indenter. Delamination occurs at 25% and 75% thickness i.e. the boundaries of ply blocks. These delaminations are elongated orthogonal to the orientation of the ply that is both adjacent to the delamination and closest to the indenter.

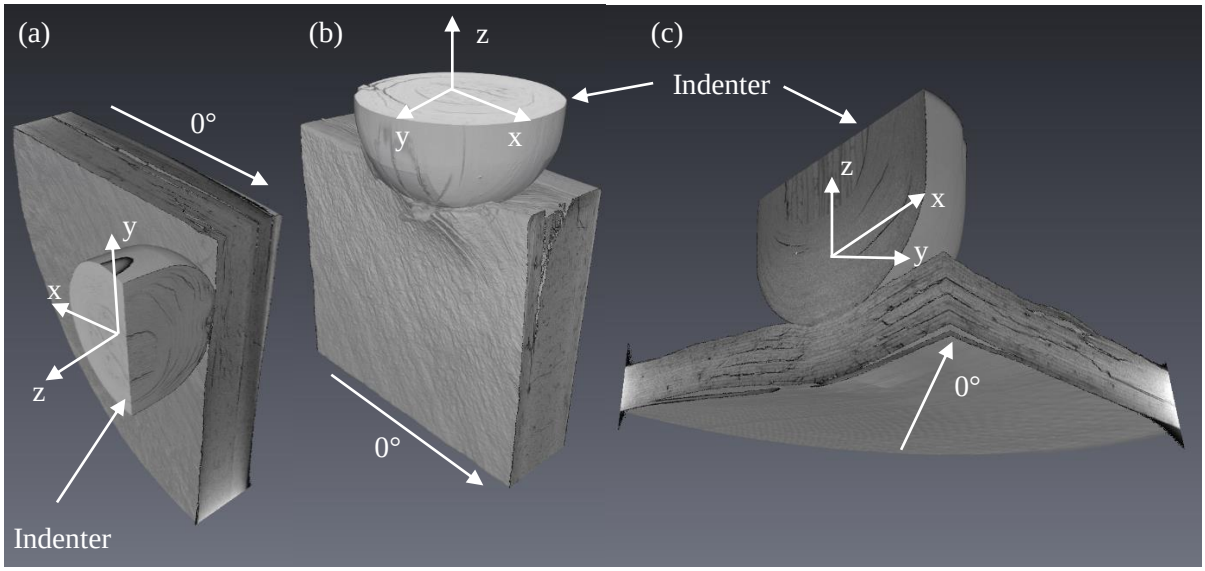

Figure 3: Three dimensional cutaway views of the 2nd indenter displacement with impact at the (a) centre, (b) on-edge and (c) near-edge locations of coupons [±45/0/90]OP, $[(\pm 60)_3]$OE and [(±45/02]NE respectively. Images are ordered as for Fig. 2.

Figures 6 and 7 show damage progression in the homogenised [±45/0/90]OP and blocked (damage tolerant) $[(\pm 45)_2]$OP coupons respectively. Comparison of Figs 6(b),(c) and (d) shows damage initiating in the form of limited delamination and shear driven intraply cracking following the first indenter displacement. Significant intra-ply cracking is also seen on the surface opposite the indenter. Following the second displacement of the indenter extensive delamination can be seen throughout the laminate (points 1-4). Delaminations are also seen to be opening and lateral growth of delaminations has been non-uniform and independent of initial delamination lengths in Fig. 6(b), see point 3 in particular. Damage progression in the $[(\pm 45)_2]$OP coupon follows a similar pattern to the [±45/0/90]OP coupon but has fewer delaminations (points 1-4) owing to the blocked stacking sequence. Greater opening of delaminations is also apparent. Parallels to a compounded version of the beam mechanism seen in the $[0_4]$OP coupon can be drawn.

Figures 8 and 9 show damage progression in the on edge indented coupons $[(\pm 60)_3]$OE and $[(\pm 45/0_2]$OE respectively. It is noted that the indenter makes contact away from the midline of the laminate and that this is the cause of the asymmetry of damage in the laminate. In the $[(\pm 60)_3]$OE coupon (Fig. 8) thermally driven intraply cracks (point 1 Figs 8(d) and (e)) are present before any indentation is applied. The thermal cracks are partially closed below the indenter following first application of displacement. The first indentation also opens a significant delamination between the blocks of ±60° and ±5° plies (point 2) that extends approximately 10mm into the laminate. The delamination appears to have been forced open by local crushing of the ±5° plies (point 3). The second displacement of the indenter causes local kink banding and further crushing of the ±5° plies (point 3), and shear failures in the now significantly deformed ±60° plies. A new delamination between the blocks of ±60° and ±5° plies is opened near the opposite surface (point 4).

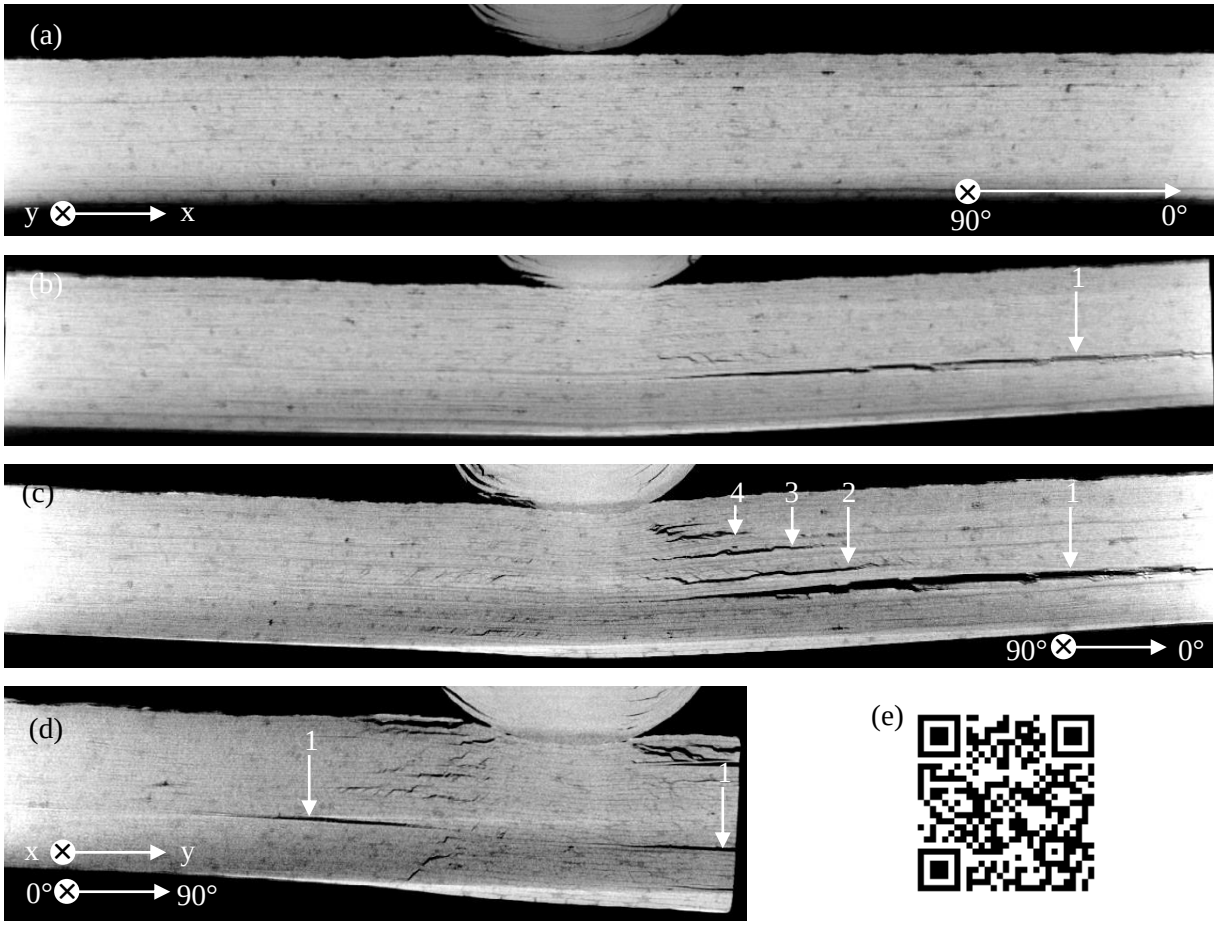

Figure 4: Cross section of [(±45/0_2]NE at the centre of impact with maximum indenter displacements of (a) 0mm, (b) 1mm, (c) 1.9mm and (d) slice orthogonal to the impact centre. (e) QR code linking to videos of all tests.

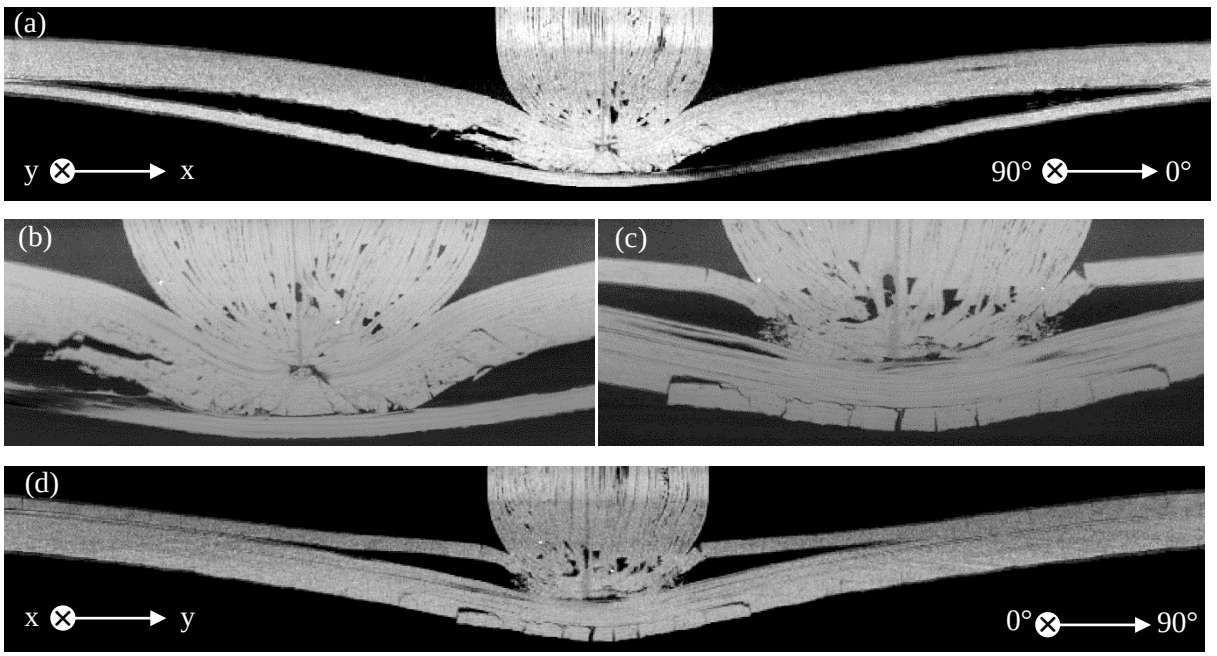

Figure 5: XRCT cross sections of [0_4]OP at the laminate mid-point held under 8kN quasi-static impact load; (a) parallel to the 0° fibres, (b) central detail parallel to 0° fibres, (c) central detail parallel to the 90° fibres, (d) parallel to the 90° fibres.

Figure 9 shows that damage progression in the $[(\pm 45/0_2]$OE coupon is similar to that seen in the $[(\pm 60)_3]$OE coupon. Delaminations are created between the ±45° surface plies and the core plies which began to crush locally under the indenter (point 2 Figs 9 (d) and (e)). The second stage of indentation causes further surface ply delamination and local crushing of the majority of the remaining plies.

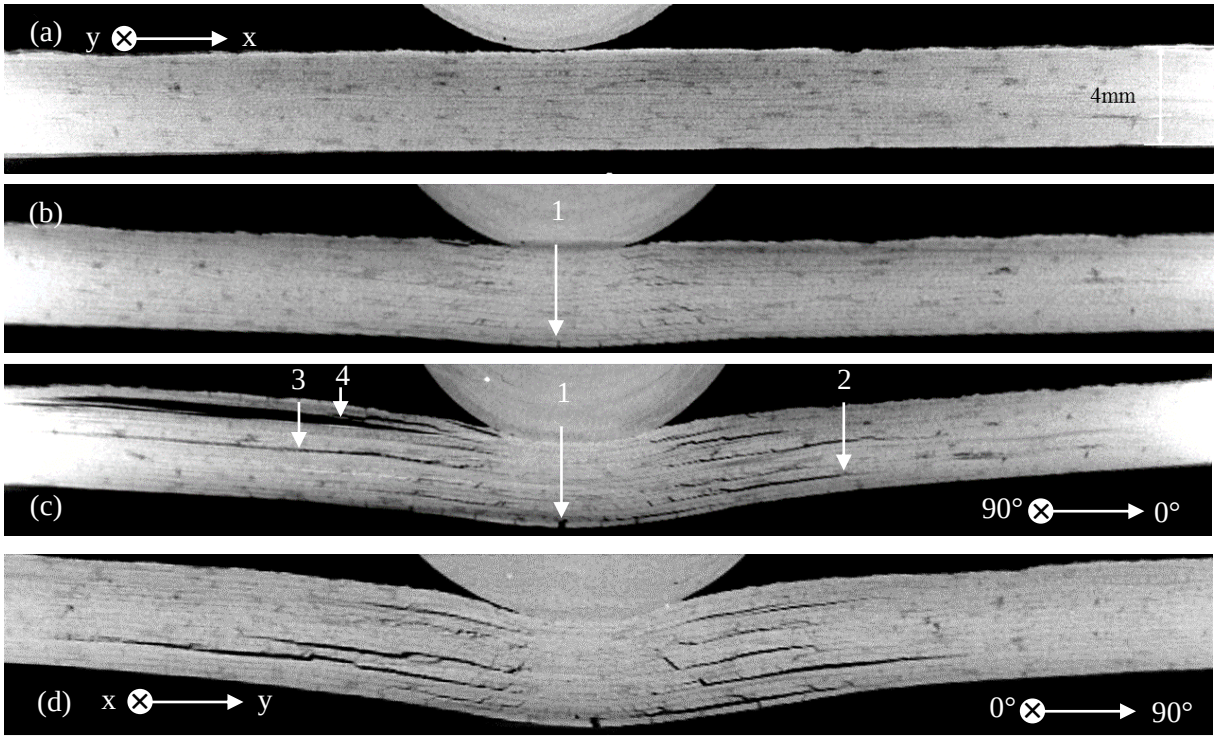

Figure 6: Central cross section of [±45/0/90]OP at the centre of impact with maximum indenter displacements of (a) 0mm, (b) 0.9mm, (c) 2.3mm and (d) slice orthogonal the centre of impact.

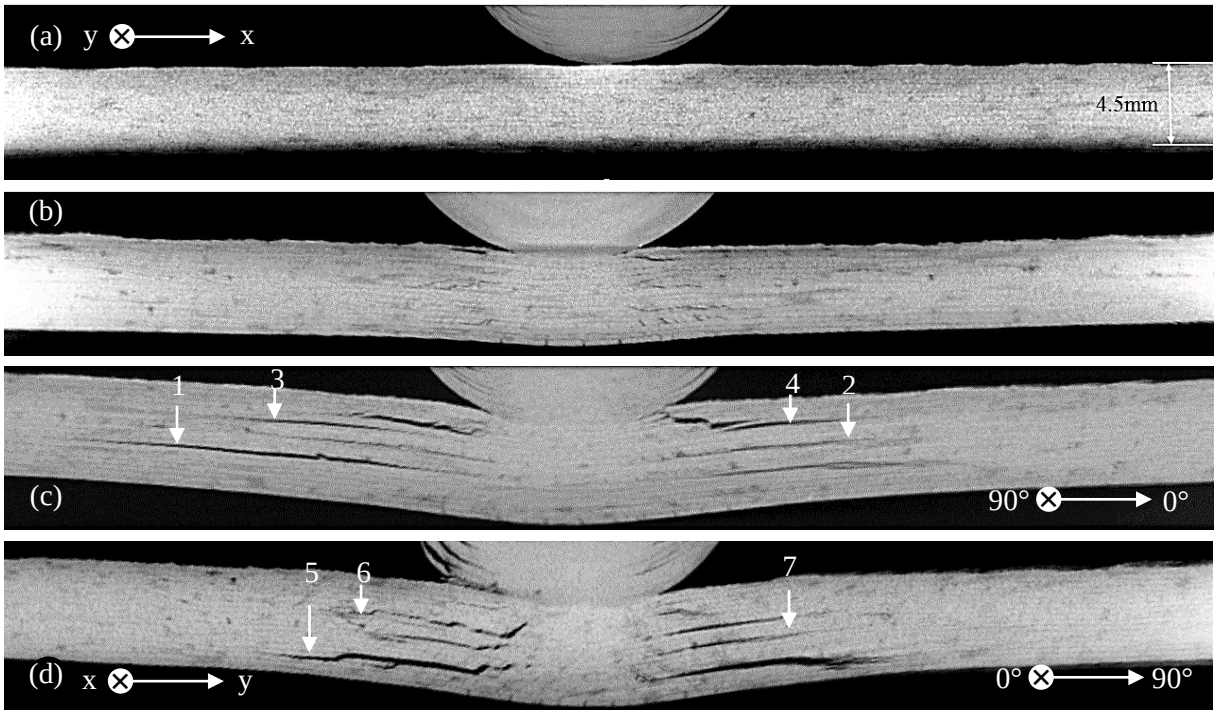

Figure 7: Central cross section of $[(\pm 45)_2]$OP at the centre of impact with maximum indenter displacements of (a) 0mm, (b) 1.1mm, (c) 1.65mm and (d) orthogonal slice at the centre of (c).

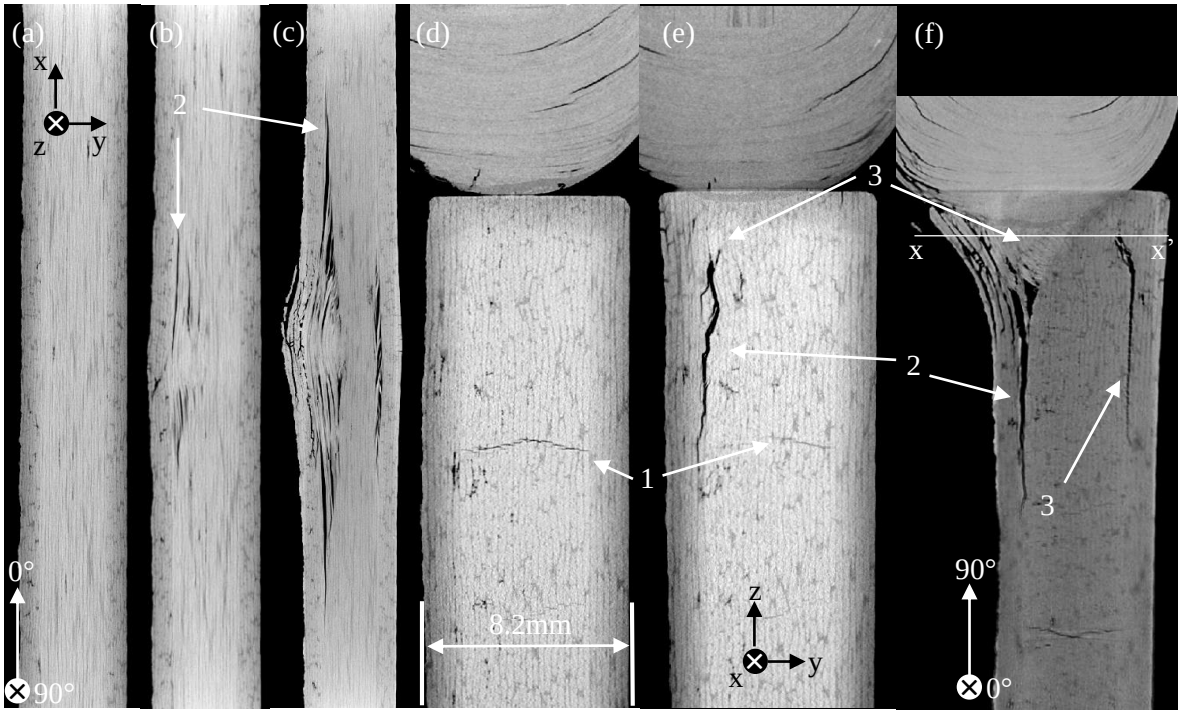

Figure 8: (a) and (d) [$(\pm 60)_3$]OE coupon in unloaded state; (b) and (e) First displacement phase = 0.8mm; (c) and (f) Second displacement = 2.08mm.

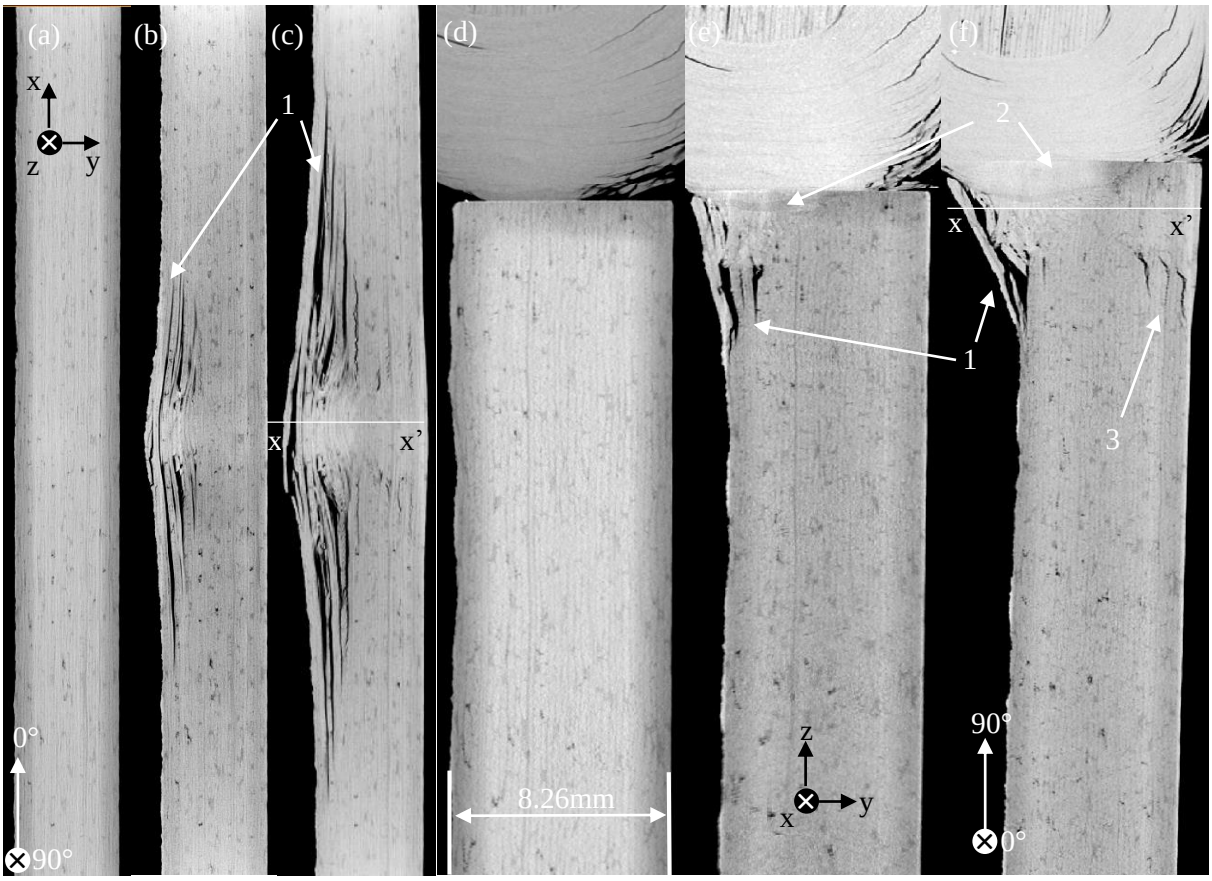

Figure 9: (a) and (d) [$(\pm 45/0_2]$OE coupon in unloaded state; (b) and (e) First displacement phase = 0.85mm; (c) and (f) Second displacement = 1.96mm.

5 DISCUSSION

Comparison of the size of different coupons' damage morphologies must be undertaken with care owing to the differing ply-percentages and indenter displacements used. Although the number of XRCT scans per coupon (and laminate stacking sequences investigated) were insufficient to make robust conclusions about the process of impact damage growth in a general laminate, a number and an order of damage formation mechanisms was nevertheless identified.

All out-of-plane impact coupons underwent two distinct stages of damage formation each with its own dominant mechanism. In the first stage (Figs 6(b) and 7(b)), damage initiates as intra-ply cracking and delamination. Delaminations occur, to some extent, at all interfaces between plies with dissimilar orientations. Delaminations are closed indicating shear driven (Mode II) fracture and have small areas. Tension driven intra-ply cracking of the surface ply opposite the impact face occurs. Crack separation distances within this ply are of the order of the tow-width within the pre-preg i.e. cracking occurs in the resin rich regions between tows, see Figs 5(c), 6(b) and 7(b).

In the second stage of damage formation (Figs 6(c) and (d), and 7(c) and (d)) delaminations open indicating a peeling (Mode I) fracture mechanism has become active. Figure 4 shows a cross-ply laminate, with maximum blocking of plies, at a large (though not unrealistic) indenter displacement. Significant peeling is caused by the impingement of a beam of plies, separated from its parent block via indenter-driven intra-ply cracking, onto a block of orthogonal plies below causing them to peel away. Such a mechanism also forms with blocked stacking sequences where ply blocks are not orthogonal, e.g. $[(\pm 45)_n/0_n]_s$. Figure 10 shows a 'hat-shaped' damage morphology (coloured region) derived from a dynamic 18J impact to a hybrid GFRP/CFRP laminate with blocked stacking sequence $[(\pm 45_C)_4/(0_g/0_c)_4]_s$, see [20,21]. Here, subscript 'g' denotes a GFRP layer and 'c' a CFRP layer. It is clear a 'beam mechanism' similar to that in Fig. 4 has driven delamination growth during impact. Comparison of Figs 4 and 10 with Fig. 7 indicates that multiple/compounded beam mechanisms are present in the second stage of damage formation in the $[(\pm 45)_2]$OP coupon. Such a mechanism was demonstrated by Bouvet al. [6] in their finite element simulations. The presence of 90° plies in the core of the $[(\pm 45)_2]$OP coupon prevents the formation of a single 'beam-mechanism' but significant, and clearly open, delaminations are present at the interface of ply blocks, see points 1-7 in Fig. 7 (c) and (d). Comparison of the second stage of damage formation in the semi-blocked $[(\pm 45)_2]$OP laminate and fully unblocked [±45/0/90]OP laminate shows that the 'beam-mechanism' has been disrupted in the latter. Although it may be present on a layer by layer basis as per Bouvet et al. [6]. Delaminations appear to show less opening, particularly in Fig. 6(c), and so it is likely that growth is a combined Mode I and II process. The even distribution of different ply-angles has created a self-supporting network of fibres that inhibits the 'beam mechanism'. This is especially as the [±45/0/90]OP laminate has undergone a significantly larger indenter displacement than the $[(\pm 45)_2]$OP coupon. However, it should be noted that further indenter displacement may lead to Mode I fracture becoming more dominant in the [±45/0/90]OP coupon. Delaminations in the $[(\pm 45)_2]$OP and [±45/0/90]OP laminate in Figs 6(c) and 7(c) respectively occur at ply interfaces where one of the adjacent plies is oriented at 0°.

Illumination of this two-stage process has two potential beneficial uses. Prudent use of ply-blocking as per Fig. 10 can lead to favourable damage morphologies which prevent near surface delaminations from forming. In the hybrid laminate of Fig. 10 this inhibited sublaminate buckling driven delamination growth and produced significantly greater residual strength than a similar CFRP only laminate [20,21]. Modelling of damage formation may be simplified by assuming first stage damage growth has already occurred. This removes the difficult task of predicting damage initiation and should be a reasonable approximation for higher energy impacts where stage two growth dominates.

Near edge impact of the $[(\pm 45/0_2]$NE coupon shows a similar two stage damage process with the exception of the significant central delamination seen in Fig. 5(c). It is unclear whether this delamination has been caused by a free-edge failure, especially as no other coupon is available for comparison at the time of writing. Significant opening of this delamination in the second stage of indenter displacement

does, however, hint that a 'beam-mechanism' may be at play. As seen by Pavier et al [8] delamination seems to be significantly large for near-edge impacts.

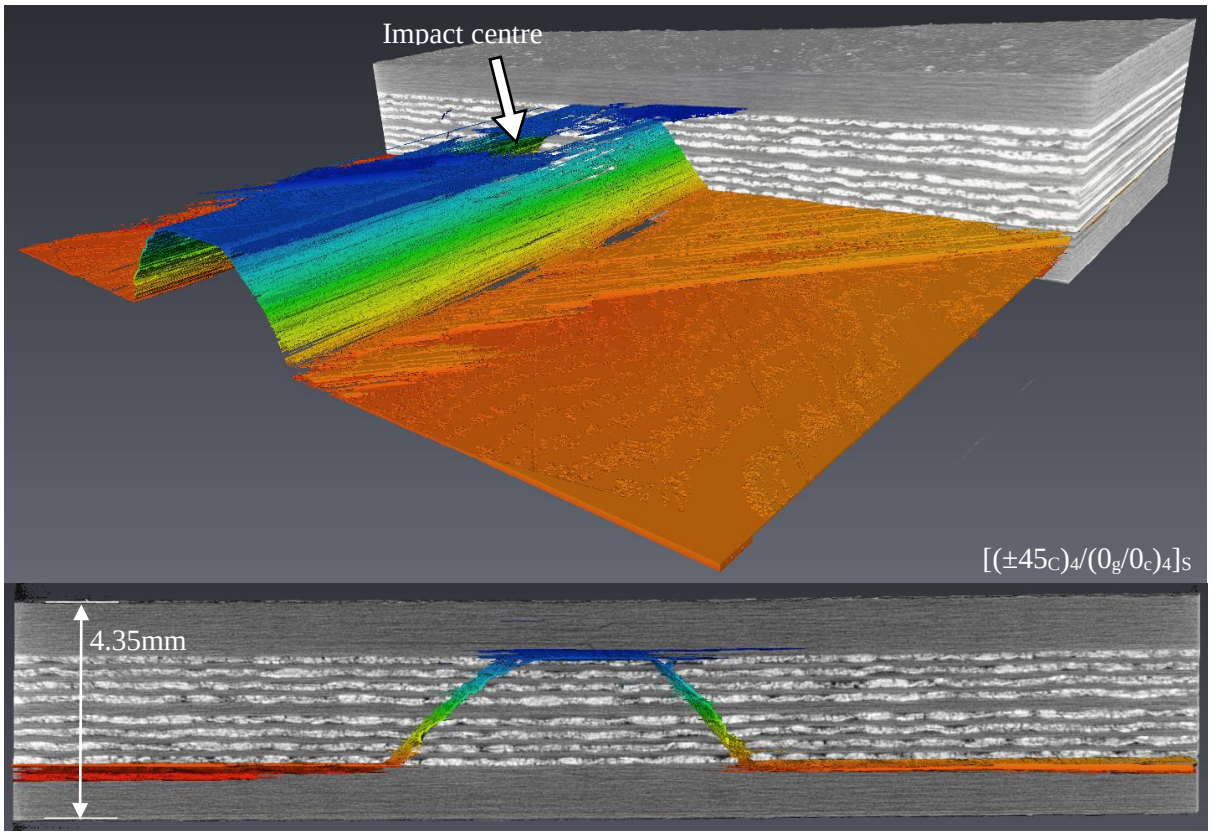

Figure 10. X-ray CT 3D distribution and cross-section of delaminations and intraply cracks following an 18J impact to a $[(\pm 45_C)_4/(0_g/0_c)_4]_s$ laminate. White layers are GFRP. Colours are indicative of delamination depth. Impact is to the top of the coupon. Scales are approximate.

Parallels in the damage formation mechanisms caused by blocking in the out-of-plane and on-edge coupons can be drawn with large delaminations occurring at the interfaces of ply-blocks. However, in both the $[(\pm 60)_3]$OE and $[(\pm 45/0_2]$OE laminates there is no clear two-stage process. Instead, crushing of plies directly below the indenter leads to outer plies being forced out-of-plane and causing them to peel away from the core plies. In the $[(\pm 60)_3]$OE laminate this only occurs at the interface of ply blocks (near both surfaces at the second indenter displacement) meaning that core load carrying 5° plies are protected from delamination. However, during the second stage of indenter displacement in the $[(\pm 45/0_2]$OE laminate, delaminations begin to occur next to all vertically oriented plies, see the right hand side of Figs 9 (c) and (f). Thermal cracks in the block of ±5° layers at the core of the $[(\pm 60)_3]$OE laminate appear to have had no effect on the formation of impact damage.

During the test program, the indenter sustained some damage, see Figs 8 and 9. As a result, the contact surface area was not constant and the stresses at the point of contact may have differed between various load stages and coupons. Displacements were, however, accurately measured using the impacted surface displacement of the coupon relative to its unloaded position.

6 CONCLUSIONS AND FUTURE WORK

In-situ X-ray Computed Tomography of the quasi-static indentation of CFRP laminates is shown to be a promising technique for investigating the mechanisms that drive the development of damage morphologies.

Damage formation in coupons subject to out-of-plane impact is seen to occur in two stages. In the first stage damage initiates in the form of intraply cracks with the addition of asymmetric and unstable growth of damage most likely driven by edge stresses in the near edge impact case. The second stage of damage formation sees a Mode I fracture component develop as a consequence of intact beams of plies impinging on blocks with dissimilar interfaces below. This 'beam-mechanism' is found to be particularly dominant in laminates of a blocked design, e.g. $[0_4/90_4]_S$. It is noted that blocking can be used to structure damage in a way which restricts significant delamination to non-critical locations in the laminate. In particular, a comparison of the blocked and unblocked out-of-plane specimens show that the damage morphology prevented the formation of near surface delaminations. Lack of such delaminations inhibits sublaminate buckling, delaying delamination growth and improving residual strength.

Laminates subject to on-edge impact exhibited a single mechanism for damage formation. Central plies were crushed forcing surface plies to peel away resulting in both Mode I and II fracture in the latter. Comparison of damage in a novel blocked stacking sequence $[(\pm60)_3/(\pm5)_5]_s$ with that in an homogenised $[(\pm45/0_2/90/0_2)_2/\pm45]_S$ sequence indicates that stacking sequence can again be used to force the development of favourable damage morphologies that protect the load carrying plies and prevent near surface delaminations.

Future work will involve experiments with a higher temporal resolution per sample by increasing the number of intermediate displacement stages. Experiments will focus on the second stage of damage formation and its progression. The on-edge impact rig configuration will be modified to better align the mid-plane of the laminate and indenter centre line. The second stage of damage formation will be the focus thus removing the need for its initiation.

REFERENCES

[1] C. S. Lopes et al., Low-velocity impact damage in dispersed stacking sequence laminates. Part II: Numerical simulations. *Composites Science and Technology* **69**(7-8), (2009), pp. 937-947. ISSN: 0266-3538. DOI: http://dx.doi.org/10.1016/j.compscitech.2009.02.015.

[2] D.J. Bull et al., A comparison of multi-scale 3D X-ray tomographic inspection techniques for assessing carbon fibre composite impact damage. *Composites Science and Technology* **75**, (2013), pp. 55-61. ISSN: 0266-3538. DOI: http://dx.doi.org/10.1016/j.compscitech.2012.12.006.

[3] S. R. Swanson, Limits of quasi-static solutions in impact of composite structures, *Composites Engineering*, **2**(4), (1992), pp. 261–267.

[4] H. Kaczmarek and S. Maison, Comparative ultrasonic analysis of damage in CFRP under static indentation and low-velocity impact, *Composites Science and Technology*, **51**(1), (1994), pp. 11-26.

[5] A. T. Nettles and M. J. Douglas, A Comparison of Quasi-Static Indentation to Low-Velocity Impact, (2000), NASA Technical Publication NASA/TP-2000-210481.

[6] C. Bouvet, B. Castanié, & J. J. Barrau, Modelling of impact damage in laminated composites. *Proceedings of 13th European Conference on Composite Materials*, (2008), Stockholm, Sweden.

[7] V. V. Bolotin, Delaminations in composite structures: its origin, buckling, growth and stability. *Composites Part B: Engineering*, **27**(2), (1996), pp. 129-145.

[8] C. Breen, F. Guild and M. Pavier, Impact damage to thick carbon fibre reinforced plastic composite laminates. *Journal of materials science*, **41**(20), (2006), pp. 6718-6724.

[9] A. Malhotra, F. J. Guild, & M. J. Pavier, Edge impact to composite laminates: experiments and simulations. *Journal of materials science*, **43**(20), (2008), pp. 6661-6667.

[10] D. Liu, Impact-induced delamination – A view of bending stiffness mismatching. *Journal of composite materials*, **22**(7), (1988), pp. 674-692.

[11] R. Olsson, Closed form prediction of peak load and delamination onset under small mass impact. *Composite Structures*, **59**(3), (2003), pp. 341-349.

[12] R. Olsson, M. V. Donadon, & B. G. Falzon, Delamination threshold load for dynamic impact on plates. *International Journal of Solids and Structures*, **43**(10), (2006), pp. 3124-3141.

[13] D. Liu, & X. Li, An overall view of laminate theories based on displacement hypothesis. *Journal of composite materials*, **30**(14), (1996), pp. 1539-1561.

[14] M. O. W. Richardson, & M. J. Wisheart, Review of low-velocity impact properties of composite materials. *Composites Part A: Applied Science and Manufacturing*, **27**(12), (1996), pp. 1123-1131.

[15] A. T. Rhead et al., Compression after impact strength of a buckling resistant tow steered panel. *19th International Conference on Composite Materials (ICCM19)*, (2013), Montreal, Canada.

[16] P. F. Giddings et al., Bistable composite laminates: Effects of laminate composition on cured shape and response to thermal load, *Composite Structures*, **92**, (2010), pp. 2220-2225. ISSN: 0263-8223. DOI: http://dx.doi.org/10.1016/j.compstruct.2009.08.043.

[17] A.T. Rhead, R. Butler and N. Baker, Analysis and compression testing of laminates optimised for damage tolerance, *Applied Composite Materials*, **18**(1), (2011), pp. 85-100. DOI: http://dx.doi.org/10.1007/s10443-010-9153-z

[18] M. U. Kismarton, (2014), Composite stiffeners for aerospace vehicles. US patent 8,720,825. URL: http://www.google.co.uk/patents/US8720825.

[19] FEI Corporate Headquarters, 5350 NE Dawson Creek Drive, Hillsboro, Oregon 97124 USA. URL: www.fei.com/software/avizo3d/

[20] A. T. Rhead, S. Hua and R. Butler, Damage resistance and damage tolerance of hybrid carbon-glass laminates, Composites Part A: Applied Science and Manufacturing, (under review).

[21] A. T. Rhead, S. Hua and R. Butler, Damage resistance and damage tolerance of hybrid carbon-glass laminates, *52nd AIAA Structural Dynamics and Materials Conference*, Denver, Colorado, USA, April 4-7, 2011.